Demonstration of Fault-Tolerant Steane Quantum Error Correction

Lukas Postler,[1,*] Friederike Butt,[2,3] Ivan Pogorelov,[1] Christian D. Marciniak,[1] Sascha Heußen,[2,3] Rainer Blatt,[1,4,5] Philipp Schindler,[1] Manuel Rispler,[2,3,†] Markus Müller,[2,3] and Thomas Monz[1,4]

[1] *Institut für Experimentalphysik, Universität Innsbruck, 6020 Innsbruck, Austria*

[2] *Institute for Quantum Information, Rheinisch-Westfälische Technische Hochschule (RWTH) Aachen University, 52056 Aachen, Germany*

[3] *Institute for Theoretical Nanoelectronics (PGI-2), Forschungszentrum Jülich, 52428 Jülich, Germany*

[4] *Alpine Quantum Technologies GmbH, 6020 Innsbruck, Austria*

[5] *Österreichische Akademie der Wissenschaften, Institut für Quantenoptik und Quanteninformation, 6020 Innsbruck, Austria*

(Received 8 February 2024; accepted 13 June 2024; published 7 August 2024)

Encoding information redundantly using quantum error-correcting (QEC) codes allows one to overcome the inherent sensitivity to noise in quantum computers to ultimately achieve large-scale quantum computation. The Steane QEC method involves preparing an auxiliary logical qubit of the same QEC code as used for the data register. The data and auxiliary registers are then coupled with a logical controlled-NOT (CNOT) gate, enabling a measurement of the auxiliary register to reveal the error syndrome. This study presents the implementation of multiple rounds of fault-tolerant (FT) Steane QEC on a trapped-ion quantum computer. Various QEC codes are employed and the results are compared to a previous experimental approach utilizing flag qubits. Our experimental findings show improved logical fidelities for Steane QEC and accompanying numerical simulations indicate an even larger performance advantage for quantum processors limited by entangling-gate errors. This establishes experimental Steane QEC as a competitive paradigm for FT quantum computing.

DOI: 10.1103/PRXQuantum.5.030326

I. INTRODUCTION

Quantum computing has the potential to outperform classical machines by exploiting superposition and entanglement. Quantum information is, due to unavoidable residual coupling of quantum systems to the environment, intrinsically prone to errors that potentially jeopardize the computational advantages promised by quantum computing. Therefore, to achieve the goal of enhanced computational capabilities, it is crucial to safeguard quantum information, e.g., by encoding it into stabilizer codes that protect against environmental and operational noise. By repeatedly measuring the stabilizer generators, we can detect noise without disrupting the logical computational state. The error and its location within the register are mapped onto the results of the stabilizer measurements, also referred to as error syndrome. We must prevent the spread of errors by following the principles of fault-tolerant (FT) circuit design, as defined in Sec. II, to conduct quantum computation on the encoded level while maintaining the expected scaling of logical error rates with physical error rates. This requirement implies experimental challenges in FT logical-state preparation, FT logical gates, and FT error correction.

Recent progress in achieving error-corrected universal quantum computation has been made through the development of FT quantum error-correcting (QEC) components in leading hardware architectures. In superconducting systems, significant strides have been made toward operating Kitaev's surface code, resulting in an operation fidelity that exceeds the break-even point [1–4]. Additionally, FT magic state preparation has been demonstrated in a superconducting experiment with fidelity beyond break-even [5]. Ion-trap experiments have demonstrated FT stabilizer readout [6], FT control of single logical qubits [7], and FT repetitive QEC cycles [8], with subsequent efforts aimed at implementing universal FT logical-gate sets [9,10]. Meanwhile, practical experimental benefits of fault tolerance

*Contact author: lukas.postler@uibk.ac.at

†Contact author: rispler@physik.rwth-aachen.de

have been demonstrated in error-detecting codes, such as FT non-Clifford gates on multiple logical qubits in both superconducting and trapped-ion devices [11], FT one-bit addition as a small logical algorithm on three logical qubits [12], the realization of Grover search utilizing encoded qubits in a trapped-ion device [13], and the very recent demonstration of a larger logical quantum processor with neutral atoms [14].

The backbone of the successful operation of an FT quantum processor is an efficient implementation of QEC cycles. Steane QEC minimizes the coupling between data and auxiliary qubits and therefore also perturbations of the data register. Thus it is a promising candidate for the efficient extraction of error syndromes on scalable error-correcting codes.

II. FAULT-TOLERANT QUANTUM ERROR CORRECTION

Given operations acting on logically encoded qubits, such as initialization, gate operations, and measurements, have to be constructed in a way that prevents dangerous propagation of errors. An error configuration is dangerous when an otherwise correctable number of errors spreads via entangling gates and turns into an error supported on a number of qubits (referred to as the weight of the error) beyond the number of errors that the code can correct. A circuit where this is precluded by design is called an FT implementation and hence we refer to the corresponding operations as FT. In particular, this applies to the QEC block itself, where the necessary coupling to auxiliary qubits unavoidably feeds back to the data qubits. Any coupling can then potentially induce errors if the auxiliary qubit or the coupling itself is faulty. A method to extract the error syndrome, which minimizes the interaction between the logical data qubit(s) and the auxiliary qubit(s), has been formulated by Steane [15]. The key idea is to prepare an auxiliary *logical* qubit using the same code as the data qubit and to couple both logical qubits via a transversal logical controlled-NOT (CNOT) gate, i.e., in a bit-wise manner. This guarantees that if any single physical operation is faulty, at most one error per encoded logical qubit block is introduced. Specifically, first, an auxiliary logical qubit is prepared in a superposition of its basis logical states $|+\rangle_L = \frac{1}{\sqrt{2}}(|0\rangle_L + |1\rangle_L)$ and a transversal $\mathrm{C}^{\mathrm{data}}\mathrm{NOT}^{\mathrm{aux}}$ is applied, as illustrated in Fig. 1(a). In the error-free case, the CNOT gate will act trivially on both encoded qubits as $\mathrm{CNOT}_L|\psi\rangle_L|+\rangle_L = |\psi\rangle_L|+\rangle_L$. However, if a single bit flip is present on the ith qubit comprising the logical data qubit [denoted as (X_i^{data})], this will be copied onto the ith qubit comprising the logical auxiliary qubit [denoted as (X_i^{aux})], as

$$\begin{aligned}&\mathrm{CNOT}_L(X_i^{\mathrm{data}} \otimes \mathbb{1})|\psi\rangle_L \otimes |+\rangle_L \\ &= X_i^{\mathrm{data}}|\psi\rangle_L \otimes X_i^{\mathrm{aux}}|+\rangle_L. \end{aligned} \tag{1}$$

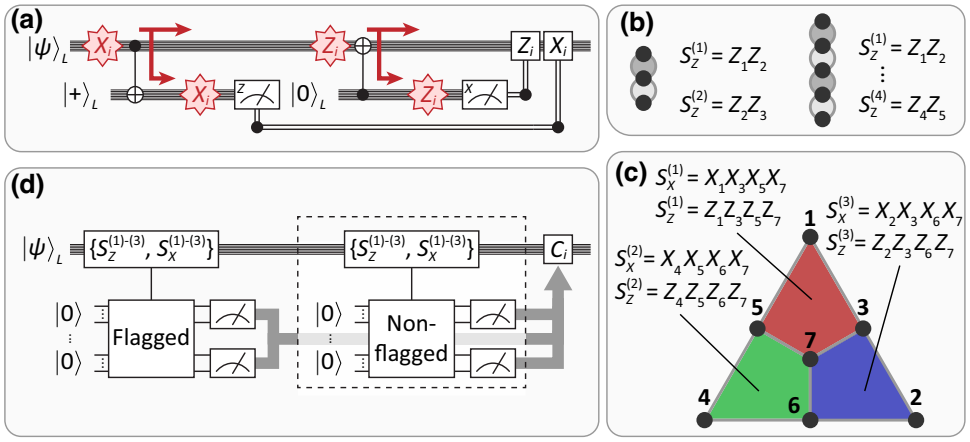

FIG. 1. Quantum error-correction codes and methods for syndrome extraction. (a) In Steane-type error correction, an auxiliary logical qubit is prepared in $|+\rangle_L$, then coupled to the initial logical qubit $|\psi\rangle_L$ with a transversal controlled-NOT (CNOT) gate, and then measured in the computational basis. This procedure is repeated for an auxiliary logical qubit in $|0\rangle_L$ with an inverted transversal CNOT gate. A correction is applied to the corresponding data qubits based on the syndrome that is extracted from the measurements performed on the auxiliary logical qubit. (b) The repetition code encodes one logical qubit and its stabilizer generators are weight-2 Pauli operators defined between neighboring qubits on a line. (c) The seven-qubit color code encodes one logical qubit into seven physical qubits. A code state is a $+1$ eigenstate of all six weight-4 stabilizer generators $\{S_X^{(i)}, S_Z^{(i)}\}$, defined on the colored plaquettes. Pauli-X (-Z) on all qubits corresponds to the logical operator X_L (Z_L), which is up to multiplication with stabilizer generators equivalent to weight-3 operators. (d) Flag error correction includes the measurement of the stabilizer generators with flagged circuits. In case of nontrivial measurement outcomes of the flagged circuits, repeating the measurement of the stabilizer generators is necessary. Different variants of flag-based QEC require different numbers of simultaneously available auxiliary qubits and remeasuring procedures. The flag QEC procedure used in this work is described in Appendix A 1.

The transversal CNOT gate is FT by construction, since it introduces at most one error on each encoded block. The entire circuit is therefore FT if one additionally verifies that only a correctable number of errors is present on the auxiliary logical qubit. The syndrome can then be reconstructed from the outcomes of the projective measurement of the auxiliary logical qubit in a single shot. One can identify the appropriate recovery operation based on a decoder such as the look-up table for the seven-qubit color, shown as Table I in Appendix A 1. Just as an auxiliary logical qubit in $|+\rangle_L$ detects propagated X errors, it detects propagated Z errors when prepared in $|0\rangle_L$ and acted upon with a transversal $\mathrm{C^{aux}NOT^{data}}$ in a second half-cycle. In this second half-cycle, Z errors are copied from the data qubit to the auxiliary qubit such that measuring the auxiliary qubits reveals the entire X syndrome simultaneously, just as the first half-cycle reveals the entire Z syndrome. This Steane-type QEC is to be seen in contrast to measuring each stabilizer individually, where due to fault-tolerance requirements one has to resort to either verified Greenberger-Horne-Zeilinger (GHZ) states or flag schemes for the auxiliary qubits [16,17]. Moreover, the syndrome measurement has to be repeated for specific measurement outcomes to avoid single faults leading to high-weight errors, which requires the conditional execution of circuits. In our experiment and simulation, in order to benchmark against the Steane-type QEC, we implement the flagged syndrome-extraction protocol of Ref. [18], which has previously been realized experimentally in [8]. The circuits that are used in the implementation are shown in Fig. 8.

In this paper, we report the implementation of Steane syndrome extraction in a trapped-ion experiment. Central to the implementation of Steane QEC is the transversal logical CNOT, which in our experiment can be performed between all qubits owing to all-to-all qubit connectivity. Transversal CNOT gates have already been demonstrated in a trapped-ion experiment [10] and even their error-propagation properties have been exploited in a neutral-atom quantum processor [14]. In this work, we employ transversal CNOT gates to repeatedly perform single-shot syndrome extraction on different error-correcting codes. As a first step, we investigate the bit-flip and phase-flip repetition codes with code distances 3 and 5 each. While the repetition code protects only against either Pauli-X or -Z errors, the syndrome-extraction procedure is the same as for leading QEC codes such as surface and color codes. We can therefore experimentally explore the scaling of Steane quantum error correction for codes of increasing distance. Furthermore, we demonstrate Steane syndrome extraction for a complete quantum error-correcting code by applying it to the seven-qubit color code. We perform up to five and three full cycles of syndrome extraction for the repetition code and the seven-qubit color code, respectively.

III. EXPERIMENTAL SETUP

All the experimental results presented in this paper have been implemented in a trapped-ion quantum processor. Sixteen $^{40}Ca^{+}$ ions are trapped in a macroscopic linear Paul trap, where the electronic state of the ions is controlled via laser pulses, as illustrated in Fig. 2(a). Each ion encodes one qubit in the electronic states $|0\rangle = |4^2S_{1/2}, m_J = -1/2\rangle$ and $|1\rangle = |3^2D_{5/2}, m_J = -1/2\rangle$ [see Fig. 2(b)], connected via an optical quadrupole transition at a wavelength of 729 nm. Coulomb interaction between the ions gives rise to collective motional modes of the ions, which are used to mediate entangling operations between any desired pair of qubits. The available universal gate set and its error characteristics are described in more detail in Appendix C.

For the repeated application of QEC blocks to encoded qubits, it is necessary to have the ability to extract the error syndrome by performing measurements on a subset of qubits. Measurements on these auxiliary qubits are designed in a way that minimizes the perturbation of the logical information stored in the data qubits. Furthermore, it is beneficial to have the capability to reuse measured qubits by reinitializing them to a defined state in the computational subspace, especially with the limited quantum register sizes of noisy intermediate-scale quantum devices. Viable approaches to implement these procedures in trapped-ion quantum processors are introducing a second atomic species [20–22], or moving ions to a distinct region of the trap [6,23] for midcircuit measurements, allowing state readout of auxiliary qubits while keeping data qubits unperturbed. In this work, we make use of multiple Zeeman sublevels in the states $|4^2S_{1/2}\rangle$ and $|3^2D_{5/2}\rangle$ (see Fig. 2) for the implementation of midcircuit measurements and subsequent reinitialization [24–26].

The first step of this procedure is the detection of the auxiliary qubits by electron shelving [27]. All data qubits are encoded in the states shown as blue symbols in Fig. 2(b) to retain the phase relation of data-qubit-superposition states and to prevent scattering out of the computational subspace. Scattering photons from auxiliary qubits projected to $|0\rangle$ heat up the ion string; therefore, a Doppler-cooling pulse, acting on the same atomic transition as also used for auxiliary-qubit-state detection, is applied. However, further cooling close to the motional ground state using resolved side-band cooling [27] is necessary for the implementation of high-fidelity gates after midcircuit measurements. The side-band-cooling procedure involves illumination with laser light that would lead to incoherent relaxation of both states marked with blue symbols to the respective ground states marked as red symbols. Therefore, the data-qubit encoding is coherently transferred to the two Zeeman sublevels of the ground state portrayed as red symbols in Fig. 2(b). Subsequent to side-band cooling, a final optical-pumping step is used

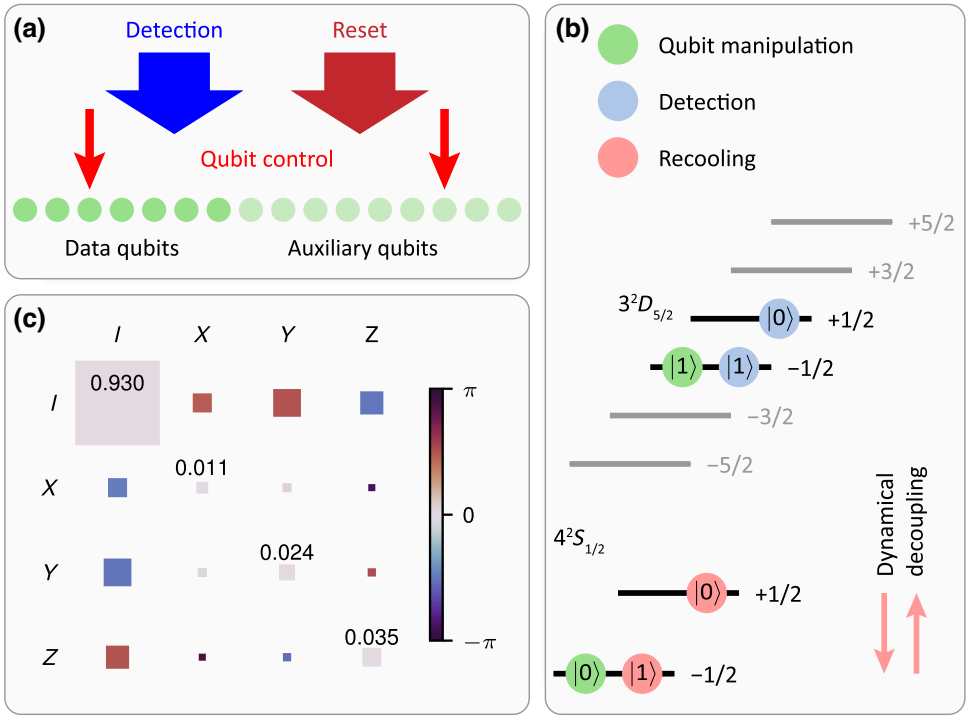

FIG. 2. Experimental methods for midcircuit measurements. (a) The qubit register is split into data-qubit and auxiliary-qubit segments. Tightly focused laser beams addressing up to two individual ions simultaneously are available to manipulate the optical qubit, while qubit-state detection and reset lasers illuminate the entire register. (b) Different qubit encodings are used prior to and during different steps of the midcircuit measurement procedure, as illustrated by the differently colored symbols. For qubit manipulation, the qubits are encoded in two Zeeman sublevels of two different electronic states (green). The data-qubit encoding is transferred to two Zeeman sublevels of the same electronic state to either decouple from laser light used to project to the computational basis during midcircuit measurements (blue) or be able to perform recooling on auxiliary qubits after a midcircuit measurement (red). While the qubit is encoded in the ground-state manifold (red), we extend the coherence time via dynamical decoupling by applying radio-frequency (rf) fields. (c) The chi-matrix representation [19] of the process acting on data qubits during midcircuit measurements, averaged over all data qubits. The area and the color coding of the squares correspond to the absolute value and the phase of an element of the chi matrix, respectively. The values on the diagonal of the averaged chi matrix are used to inform the error model (see Appendix B).

to reinitialize all auxiliary qubits that are supposed to be reused. Finally, we restore the encoding of the data qubits to the states shown as green symbols, where further gate operations on the optical qubit can be implemented. A more detailed description of the procedure can be found in Appendix C.

The duration of the midcircuit detection procedure is dominated by the side-band-cooling step with a duration on the order of the coherence time. Therefore, a dynamical decoupling sequence [28,29] is performed on the data qubits during the recooling procedure. This decoupling is implemented with a resonant radio-frequency (rf) antenna driving the transition between the two ground states on the entire register simultaneously, where the data qubits are encoded during side-band cooling (red symbols). A refocusing pulse is applied approximately every millisecond in between cooling pulses for different motional modes. In Fig. 2(c), we show the process matrix [19] of the evolution of data qubits during a full midcircuit measurement procedure, including dynamical decoupling averaged over all data qubits.

IV. STEANE QEC FOR THE REPETITION CODE AND THE SEVEN-QUBIT COLOR CODE

In this section, we show the application of Steane QEC to one-dimensional (1D) repetition codes and the two-dimensional (2D) seven-qubit color code. First, we study the scaling of Steane QEC with the code distance, by presenting results for distances 3 and 5 for both the bit- and phase-flip repetition codes. The structure of the codes and the stabilizer generators are illustrated in Fig. 1(b). Despite their simplicity, these codes share key properties, such as syndrome extraction, logical processing, and error suppression, with fully fledged topological QEC codes. Consequently, they routinely form a test bed for the latter [1,30]. One round of error correction in repetition codes consists of only one half of the cycle illustrated in Fig. 1(a),

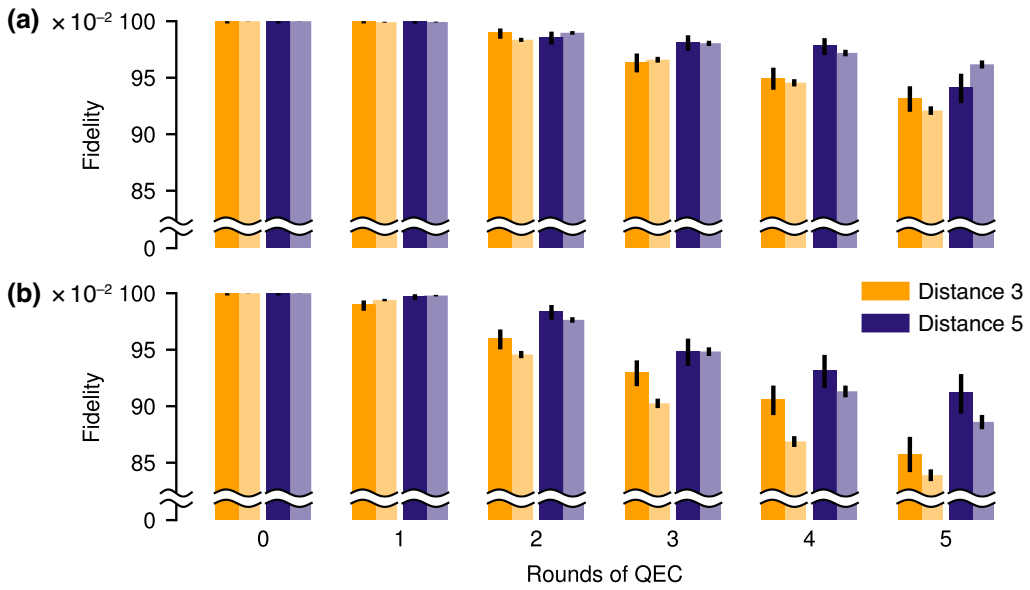

FIG. 3. Logical fidelities for bit- and phase-flip repetition code for distances 3 and 5. Fidelities for up to five rounds of Steane-type error correction for the distance-3 and distance-5 (a) bit-flip and (b) phase-flip code. Round 0 corresponds to the encoding of the logical state with no extra round of QEC. The experimental and simulation results are depicted with darker and lighter shades, respectively. The error bars shown in this and all following data figures are calculated as described in Appendix D [41].

since the codes can only correct either X or Z errors. For example, for Steane-type QEC on the distance-3 bit-flip code, a logical state $|\psi\rangle_L$ is encoded in $|000\rangle$. The auxiliary logical qubit is prepared in a three-qubit GHZ state $|+\rangle_L = (|000\rangle + |111\rangle)/\sqrt{2}$. If, for example, an X fault occurs on the first qubit, this will propagate onto the auxiliary logical qubit when the auxiliary qubit is coupled to the logical data qubit with a transversal CNOT gate. A final projective measurement of the auxiliary logical qubit in the Z basis projects the state onto either $|011\rangle$ or $|100\rangle$. We can extract the stabilizer values $S_Z^{(1)} = Z_1Z_2$ and $S_Z^{(2)} = Z_2Z_3$, as given in Appendix A 2, by checking the parity of this measurement outcome. It is then possible to identify the initial fault on the first qubit based

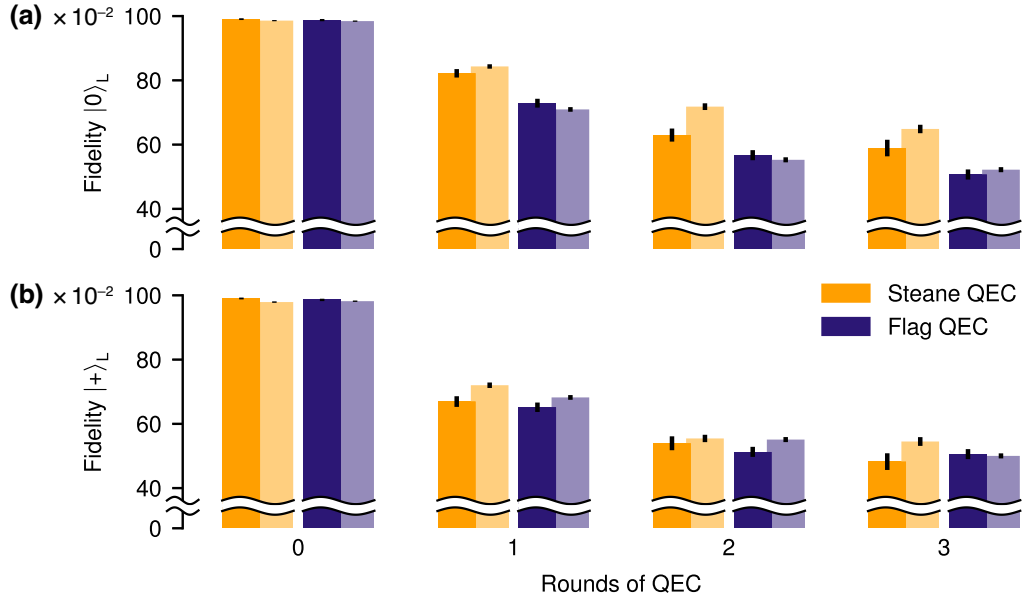

FIG. 4. Logical fidelities for syndrome extraction on the seven-qubit color code. The logical fidelities obtained from Steane-type and flag-based QEC for the logical input state (a) $|0\rangle_L$ and (b) $|+\rangle_L$. Round 0 corresponds to the encoding of the logical state with no extra round of QEC. The experimental and simulation results are depicted with darker and lighter shades, respectively.

on the syndrome $(S_Z^{(1)}, S_Z^{(2)}) = (-1, 1)$. For the distance-5 repetition code, the auxiliary logical state has to be verified to ensure that no single fault has caused a weight-2 error configuration on the auxiliary GHZ state. We do this by coupling a single flag qubit to the prepared auxiliary qubit, heralding weight-2 error configurations, as shown in Fig. 11 in Appendix A 2. No verification is required for $d = 3$, since any single fault only results in a correctable error configuration on each encoded block. The phase-flip code can be treated completely analogously to the bit-flip code. In Fig. 3, we show the probability of recovering the target logical state, within the correction capabilities of the respective QEC code, for the bit- and phase-flip code with distances $d = \{3, 5\}$. We refer to this probability as the logical fidelity (see Appendix E). Corrections suggested by the repeated syndrome extraction are accounted for via a Pauli-frame update [31]. We can identify that increasing the code distance from 3 to 5 improves the logical fidelities for both the bit- and the phase-flip code. The lower fidelities for the phase-flip code compared to the bit-flip code can be attributed to dephasing on idling qubits. The experimental results are accompanied by Monte Carlo simulations using an experimentally informed effective noise model. The model accounts for errors on single-qubit gates, two-qubit gates, qubit initialization, and measurements with error rates $p_{1q} = 3.6 \times 10^{-3}$, $p_{2q} = 2.7 \times 10^{-2}$, $p_{\text{init}} = 3 \times 10^{-3}$, and $p_{\text{meas}} = 3 \times 10^{-3}$, respectively. Furthermore, during midcircuit measurements, the remaining qubits experience noise that we model as asymmetric depolarizing noise with error probabilities $p^{(x)}_{\text{midcirc}} = 1.1 \times 10^{-2}$, $p^{(y)}_{\text{midcirc}} = 2.4 \times 10^{-2}$, and $p^{(z)}_{\text{midcirc}} = 3.5 \times 10^{-2}$, acting on all idling data qubits independently. These error probabilities are extracted from the experimental process matrix, quantifying the effect of midcircuit measurements on idling (data) qubits, shown in Fig. 2(c). A more detailed description of the error model can be found in Appendix B. The simulation data obtained with this relatively simple multiparameter incoherent noise model show good agreement with the experimental data, which indicates that the model captures the experiment well for the given error rates.

Going a step further, we now apply the above-described Steane-type QEC to the seven-qubit color code [32–34], shown in Fig. 1(c), and compare its performance to that of the previously used flag-based QEC scheme [8,9,18]. In the latter, the syndrome information is extracted by measuring stabilizers using additional auxiliary physical qubits, as illustrated in Fig. 1(d). The seven-qubit color code $[\![7, 1, 3]\!]$ is the smallest topological color code and encodes a single logical qubit while allowing the correction of a single arbitrary Pauli error. It has the highly desirable property of admitting a transversal and thus FT implementation of the entire Clifford group. Physical qubits are placed on the vertices of a 2D graph and the encoded logical qubit is defined as the simultaneous $+1$ eigenstate of the six indicated stabilizer generators. A single flag qubit is used to verify the prepared logical state such that unsuccessful preparations can be discarded [9,35] analogous to usage in the distance-5 repetition code. The encoding circuit and look-up table are given in Appendix A 1.

In Fig. 4, we show the logical fidelities that we have obtained experimentally and numerically from Monte Carlo simulations. We find an advantageous performance in terms of fidelity for the Steane-type QEC compared to the flag-based QEC scheme, where the performance benefit of the Steane QEC is more pronounced for the state $|0\rangle_L$. The reason for this asymmetry is that the dominant error source in the experimental setup at hand is asymmetric depolarizing noise on the data qubits during midcircuit measurements. Additionally, dephasing of data qubits is taking place during the implementation of gates on the auxiliary qubits (see Table III in Appendix B). This conflates the logical failure rates for the different protocols and partially veils the advantage of Steane QEC, which is most pronounced in the regime of dominating two-qubit error rates. Therefore, we estimate the projected advantage of Steane-type QEC by numerically simulating logical error rates in a setting in which the only noise source is two-qubit gate errors. In this regime, we find that the logical error rate of Steane-type QEC is suppressed by as much as a factor of 2, compared to flag-type QEC (see Fig. 9 in Appendix A 1). Experimental improvements such as an extended coherence time on the order of seconds [36–38] or composite pulses robust against laser amplitude noise and crosstalk [39,40] could further mitigate perturbations of the idling data qubits during midcircuit measurements and therefore also extend the advantage in logical fidelity offered by the Steane-type over the flag-type QEC in the present experimental setup. Additional results on the extraction of only the Z (X) syndrome for the logical state $|0\rangle_L$ ($|+\rangle_L$) are presented in Appendix F.

V. CONCLUSIONS AND OUTLOOK

In this work, we have shown the practical advantage of Steane over flag-based QEC in a noisy intermediate-scale trapped-ion quantum processor. We have implemented up to five rounds of Steane QEC for bit-flip and phase-flip repetition codes with distances 3 and 5 and observed an improvement of the logical fidelity with greater distances. This increase despite larger qubit and gate overhead per logical qubit shows that both codes have been operated below their respective thresholds. We have further demonstrated an advantage of repeated Steane QEC on the seven-qubit color code, where multiple complete rounds of error correction including repeated midcircuit measurements present substantial experimental challenges. Numerical simulations based on a multiparameter depolarizing error model, informed by experimentally estimated

error rates of basic quantum operations, underpin this finding and capture the features in the experimental data. The improved QEC performance has been achieved without the necessity of making any changes to the hardware but is rooted in the carefully crafted quantum circuit design underlying the Steane-type QEC approach. The present implementation is currently limited by errors during mid-circuit measurements. Therefore, the benefit of Steane QEC will increase up to the numerically anticipated margin of about a factor of 2 if the error rate of the mid-circuit measurement procedure becomes smaller than the entangling-gate errors.

The results presented in this work have established Steane QEC as a new paradigm in experimental QEC by showing reduced error rates of encoded qubits compared to other QEC protocols. The demonstrated Steane-type QEC approach is especially relevant in the context of the emergence of larger qubit registers with efficient implementations of entangling logical gates on various platforms. In architectures that allow for a parallel application of two-qubit gates acting on distinct subsets of qubits, a transversal CNOT gate and, therefore, the extraction of Z-type and X-type error syndromes, can each be implemented within one circuit time step. We believe that Steane QEC will play a pivotal role on the path to large-scale FT quantum computation owing to its increased logical fidelities and modularity, which will allow us to harness the emerging capabilities of efficiently and fault-tolerantly coupled logical qubits as building blocks.

Note added. Please also note the preprint entitled "Comparing Shor and Steane Error Correction Using the Bacon-Shor Code" by S. Huang, K. R. Brown, and M. Cetina on related work.

The data underlying the findings of this work are available at Ref. [41]. All codes used for data analysis are available from the corresponding author upon reasonable request.

ACKNOWLEDGMENTS

We gratefully acknowledge support by the European Union (EU) Horizon Europe research and innovation program under Grant Agreement No. 101114305 ("MILLENION-SGA1" EU Project), the U.S. Army Research Office through Grant No. W911NF-21-1-0007, the EU Horizon Europe research and innovation program under Grant Agreement No. 101046968 ["Brisk Rydberg Ions for Scalable Quantum Processors" (BRISQ)], the ERC Starting Grant QCosmo under Grant No. 948893, the ERC Starting Grant QNets through Grant No. 804247, the Austrian Research Promotion Agency under Contracts No. 896213 (Ion trap arrays for quantum computing) and No. 897481 (High-Performance integrated Quantum Computing). This research was funded in part by the Austrian Science Fund (FWF) [10.55776/F71]. For open access purposes, the authors have applied a CC BY public copyright license to any author accepted manuscript version arising from this submission. We further acknowledge funding by the Office of the Director of National Intelligence (ODNI), Intelligence Advanced Research Projects Activity (IARPA), via the U.S. Army Research Office through Grant No. W911NF-16-1-0070 under the LogiQ program, and by IARPA and the Army Research Office, under the Entangled Logical Qubits program through Cooperative Agreement No. W911NF-23-2-0216. This research is also part of the Munich Quantum Valley (K-8), which is supported by the Bavarian state government with funds from the Hightech Agenda Bayern Plus. We further receive support from the IQI GmbH and from the German Federal Ministry of Education and Research (BMBF) via the Verein Deutscher Ingenieure within the "Ion Quantum Processor with HPC Connection" (IQuAn) project, and by the Deutsche Forschungsgemeinschaft (DFG, German Research Foundation) under Germany's Excellence Strategy "Cluster of Excellence Matter and Light for Quantum Computing (ML4Q) EXC 2004/1" 390534769.

L.P. and I.P. carried out the experiments. L.P., I.P., C.D.M., P.S., and T.M. contributed to the experimental setup. L.P., F.B., and M.R. analyzed the data. F.B., S.H., and M.R. performed the numerical simulations. F.B., S.H., and M.R. performed circuit analysis, characterization, and theory modeling. L.P., F.B., I.P., C.D.M., S.H., P.S., and M.R. wrote the manuscript, with contributions from all authors. R.B., P.S., M.R., M.M., and T.M. supervised the project.

R.B. and T.M. are founders of Alpine Quantum Technologies GmbH, a commercially oriented quantum computing company.

The views and conclusions contained in this document are those of the authors and should not be interpreted as representing the official policies, either expressed or implied, of IARPA, the Army Research Office, or the U.S. Government. The U.S. Government is authorized to reproduce and distribute reprints for Government purposes notwithstanding any copyright notation herein.

APPENDIX A: QUANTUM ERROR-CORRECTING CODES

1. The seven-qubit color code

A powerful tool for describing a large group of quantum error-correction codes is the stabilizer formalism. In an n-qubit quantum system encoding k logical qubits, a group of mutually commuting Pauli operators defining a quantum error-correction code, referred to as the stabilizer, can be specified. Any valid code state is a $+1$ eigenstate with respect to all elements of the group, which can be generated by a set of $n-k$ stabilizer generators. By measuring

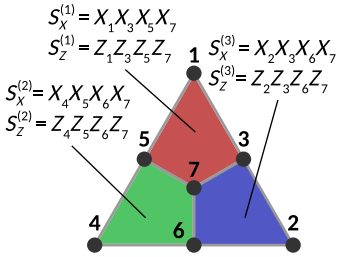

FIG. 5. The stabilizer generators of the seven-qubit color code, which encodes one logical qubit into seven physical qubits. A code state is a $+1$ eigenstate of all six weight-4 stabilizer generators $\{S_X^{(i)}, S_Z^{(i)}\}$ defined on the colored plaquettes. Pauli-X (-Z) on all qubits corresponds to the logical operator X_L (Z_L), which is, up to multiplication with stabilizer generators, equivalent to weight-3 operators.

the expectation values of the stabilizer generators, errors can be detected and subsequently corrected through quantum error-correction protocols, preserving the integrity of the encoded quantum information. The distance d of the code is given by the minimal weight of a nontrivial operator that does retain the quantum state it is acting on within the subspace of $+1$ eigenstates of the stabilizer. An n-qubit stabilizer code with a distance d encoding k qubits is commonly denoted as an $[\![n, k, d]\!]$ code.

The seven-qubit color code $[\![7, 1, 3]\!]$ is constructed by placing physical qubits on the vertices of a graph [32]. The encoded logical qubit is defined as the simultaneous $+1$ eigenstate of the six stabilizer generators,

$$\begin{aligned} S_X^{(1)} &= X_1X_3X_5X_7, \quad S_Z^{(1)} = Z_1Z_3Z_5Z_7, \\ S_X^{(2)} &= X_4X_5X_6X_7, \quad S_Z^{(2)} = Z_4Z_5Z_6Z_7, \\ S_X^{(3)} &= X_2X_3X_6X_7, \quad S_Z^{(3)} = Z_2Z_3Z_6Z_7, \end{aligned} \tag{A1}$$

TABLE I. The look-up table for the seven-qubit color code. For each syndrome measurement with a given set of positive $+$ and negative $-$ outcomes, a single-qubit recovery operation is applied. Since X and Z stabilizers are defined symmetrically on the same support, the Z-type recoveries based on the X syndrome are applied analogously. Any Y error can be considered as a combined X and Z error and be corrected independently.

$S_Z^{(1)}, S_Z^{(2)}, S_Z^{(3)}$	Recovery
$+++$	I
$-++$	X_1
$++-$	X_2
$-+-$	X_3
$+-+$	X_4
$--+$	X_5
$+--$	X_6
$---$	X_7

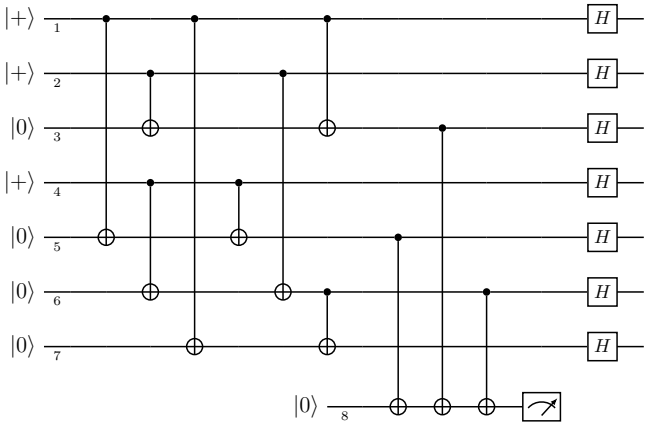

FIG. 6. The circuit for the encoding of a logical state in the seven-qubit color code [9,35]. The first eight CNOT gates initialize $|0\rangle_L$ on the seven-qubit color code. This is followed by a verification in order to detect single faults that would otherwise propagate onto multiple data qubits and cause a logical failure. Finally, a transversal application of H_L may be applied to prepare $|+\rangle_L$.

as illustrated in Figs. 1(a) and 5. The logical operators are given by $Z_L = Z^{\otimes 7}$ and $X_L = X^{\otimes 7}$, which can be expressed as weight-3 operators by multiplication with stabilizers. For instance, multiplying $S_X^{(1)}$ with X_L gives the weight-3 logical operator $X_2X_4X_6$. The circuit shown in Fig. 6 is used to encode a logical state in the seven-qubit color code [35].

In the error-free case, a measurement of the set of stabilizer generators will yield the outcome $+1$ for each one, since a valid code state is a $+1$ eigenstate of these operators. If a single Pauli fault occurs, this will anticommute with a set of stabilizers. The measurement outcomes in this case will yield the outcome -1 for a set of stabilizers. This syndrome-measurement outcome is unique to the initial single Pauli fault when excluding error configurations of weight greater than 1. Therefore, one can correct for this error and recover the code state. However, higher-weight error configurations break this uniqueness and can lead to logical errors when applying the recovery operation. For instance, the weight-1 error configuration X_5 and the weight-2 configuration X_1X_4 lead to the same Z syndrome $\{S_Z^{(1)} = -1, S_Z^{(2)} = -1, S_Z^{(3)} = 1\}$. Applying the recovery operation X_5 would lead to a logical error for the weight-2 error case, as the weight-3 configuration $X_1X_4X_5 = X_L S_X^{(3)}$ is, up to multiplication with a stabilizer generator, equivalent to X_L. Table I summarizes the possible Z-syndrome-measurement outcomes and the corresponding recovery operation, which corrects any single Pauli-X error. Since the seven-qubit color code is self-dual, i.e., symmetric under the exchange of X and Z stabilizers, the look-up table for Pauli-Z corrections based on the measured X syndrome is the same.

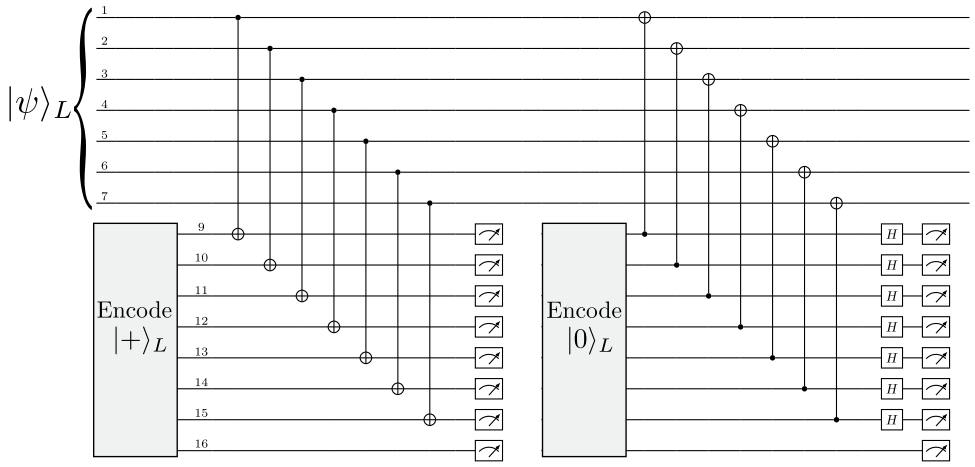

FIG. 7. The circuits for the Steane-type syndrome extraction in the seven-qubit color code [15,42,43]. A logical auxiliary qubit is initialized using the circuit shown in Fig. 6, coupled to the data qubits and measured.

The syndrome can be extracted using Steane-type QEC with the circuit shown in Fig. 7, where transversal CNOT gates copy errors onto an auxiliary logical qubit that is then measured projectively. In Fig. 8, we show the circuit that we use for flagged syndrome readout on the seven-qubit color code [8,9,18]. If no error is detected in a first round of flagged stabilizer measurements, we assume that no error has occurred and proceed. If a nontrivial syndrome is measured, the complete syndrome is measured again with unflagged circuits to distinguish the dangerous propagated flag errors from nonflag errors. If the two syndromes agree, we take this as a final syndrome for error correction with look-up Table I. If they do not agree and the unflagged syndrome coincides with a flag-error syndrome in Table II, we apply the corresponding flag-error correction. In the event that the unflagged syndrome is not in the flag look-up table, the single-qubit recovery from Table I is used. Note that while one could immediately apply the correction to the data register, it is admissible to just keep track of this in software (known as Pauli-frame tracking) as long as no logical non-Clifford gate is applied. The experimental setup currently does not allow for real-time changes of the gate sequence based on outcomes of midcircuit measurements. For the realization of flagged QEC, we experimentally implement both possible circuits, with and without a second unflagged measurement of the stabilizer generators, and all combinations thereof for multiple QEC cycles. Then we discard all measurements for which the flagged syndrome outcomes

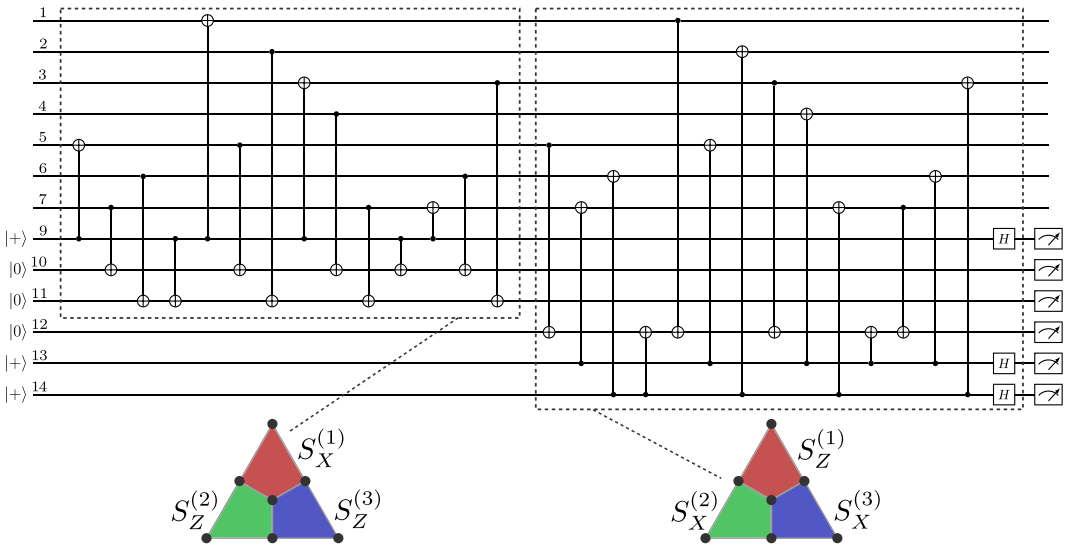

FIG. 8. The circuit for flagged syndrome readout for the syndrome extraction on the seven-qubit color code [8,9,18]. The first part of the circuit measures $S_X^{(1)}$, $S_Z^{(2)}$, and $S_Z^{(3)}$ and the second part extracts $S_Z^{(1)}$, $S_X^{(2)}$, and $S_X^{(3)}$.

TABLE II. The flag look-up table for the seven-qubit color code. If the outcomes of flagged and unflagged syndrome readouts do not agree and the measured unflagged syndrome is in this table, the corresponding recovery operation is applied. If the unflagged syndrome is not in this table, the respective single-qubit recovery operation from Table I is applied. Since the X and Z stabilizers are defined symmetrically on the same support, the Z-type recoveries based on the X syndrome are applied analogously.

$S_Z^{(1)}, S_Z^{(2)}, S_Z^{(3)}$	Recovery
$+-+$	X_3X_7
$++-$	X_4X_6

do not correspond to the selected sequence of syndrome readouts.

We numerically calculate the fidelities for the limiting case in which all error rates except p_{2q} are set to 0, as shown in Fig. 9, in order to estimate the potential advantage of Steane-type QEC over the flag-based approach. Since there is no additional dephasing included, the systematic difference in fidelity between the two logical states $|0\rangle_L$ and $|+\rangle_L$ vanishes. The fidelities for the Steane-type approach are higher than for the flag-based protocol and this difference increases with the number of QEC rounds. After two rounds of QEC, the fidelity for the Steane-type approach is already more than 0.1 higher than for the flag-based protocol. This promises an advantage of Steane-type QEC in the regime of dominating two-qubit error rates.

2. The 1D repetition code

For the n-qubit bit-flip code [19], the logical $|0\rangle_L$ is encoded in n copies of $|0\rangle$ as $|0\rangle_L = |0\rangle^{\otimes n}$. The stabilizer generators are given by pairs of neighboring Pauli-Z operators $\{Z_1Z_2, Z_2Z_3, \ldots, Z_{n-1}Z_n\}$ and the logical operators are $X_L = X^{\otimes n}$ and $Z_L = Z_1$. Analogously, the phase-flip code takes repetitions of $|+\rangle$ to encode information redundantly on multiple qubits. In this case, one can define the n-qubit state $|0\rangle_L = |+\rangle^{\otimes n}$, the stabilizers correspond to pairs of Pauli-X operators $\{X_1X_2, X_2X_3, \ldots, X_{n-1}X_n\}$, and the logical operators are given by $X_L = Z^{\otimes n}$ and $Z_L = X_1$. Steane-type QEC is performed by initializing a second logical qubit in the corresponding logical $|+\rangle_L$ and applying a transversal CNOT gate, as shown exemplarily in Fig. 11 for the distance-5 repetition code.

APPENDIX B: EFFECTIVE NOISE MODEL AND SIMULATION METHODS

In order to estimate the logical fidelities of the discussed error-correction protocols, we perform Monte Carlo simulations using the STIM [44] and PECOS [45] software. Every component in a circuit is modeled as an ideal operation U_{ideal} followed by an error E drawn from an error set with a given probability p. We consider depolarizing noise

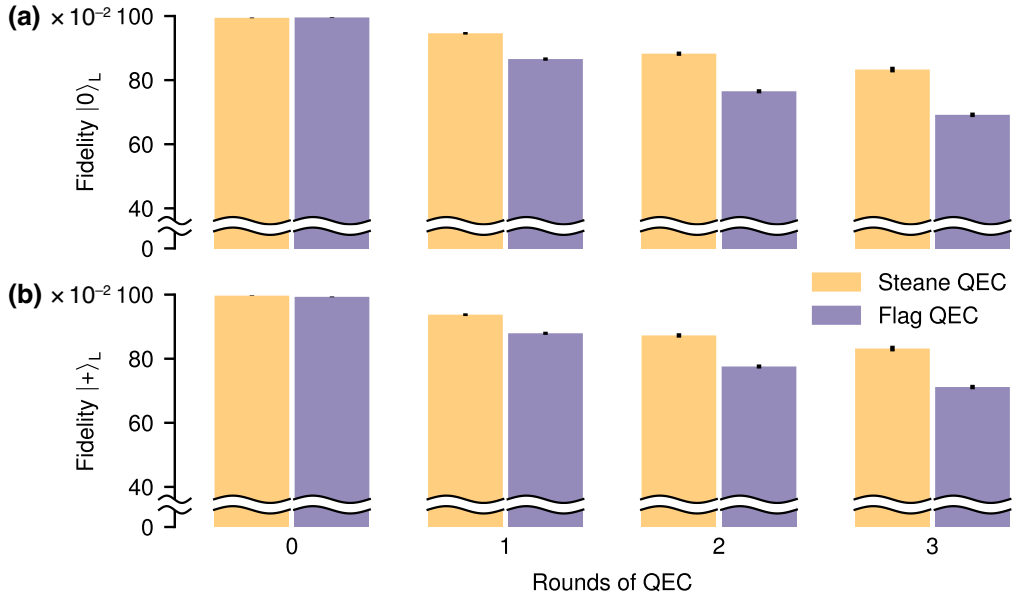

FIG. 9. Fidelities from numerical simulations for Steane-type and flagged syndrome extraction in the limiting case of only accounting for two-qubit gate errors. All error probabilities, apart from the two-qubit gate error probability $p_{2q} = 0.025$, are set to $p_{1q} = p_{\text{init}} = p_{\text{meas}} = p_{\text{midcirc}} = 0$. Shown are the logical fidelities for the seven-qubit color code after preparing the logical states (a) $|0\rangle_L$ and (b) $|+\rangle_L$. Steane-type QEC reaches higher fidelities than the flag-based approach and this difference increases with the number of subsequent rounds of QEC. Round 0 corresponds to the encoding of the logical state with no extra round of QEC.

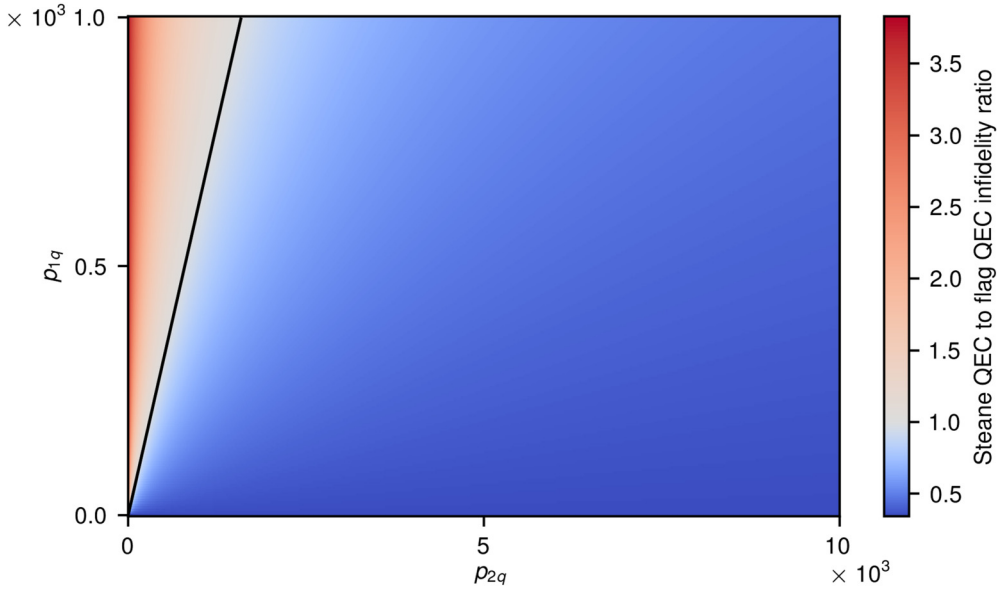

FIG. 10. The infidelity ratio from numerical simulations for Steane-type and flagged syndrome extraction in the limiting case of small two-qubit and single-qubit gate errors. All error probabilities, apart from the gate errors p_{2q} and p_{1q}, are set to $p_{\text{init}} = p_{\text{meas}} = p_{\text{midcirc}} = 0$. We calculate the leading order in the infidelity for both schemes by performing fault-path counting (see Appendix B) on the respective circuits. We plot the infidelity ratio of Steane-type over flagged syndrome extraction, such that values below (above) 1 indicated in blue (red) indicate an advantage for Steane-type (flagged) syndrome extraction. The black line indicates the contour of equal infidelity of Steane-type and flagged QEC. The results of our simulations show that when the two-qubit gate error is dominant ($p_{2q} \gg p_{1q}$), Steane-type syndrome readout also offers an advantage at low physical error rates.

channels on single- and two-qubit gates,

$$\begin{aligned}\mathcal{E}_1(\rho) &= (1-\sum_{j=1}^{3} p_j)\rho + \sum_{j=1}^{3} p_j E_1^j \rho E_1^j \\ \mathcal{E}_2(\rho) &= (1-p_{2q})\rho + \frac{p_{2q}}{15}\sum_{j=1}^{15} E_2^j\, \rho\, E_2^j,\end{aligned} \tag{B1}$$

with the error sets

$$\begin{aligned}E_1 &\in \{\sigma_k, \forall k \in \{1,2,3\}\}, \\ E_2 &\in \{\sigma_k \otimes \sigma_l, \forall k,l \in \{0,1,2,3\}\}\backslash\{\sigma_0 \otimes \sigma_0\},\end{aligned} \tag{B2}$$

where the σ_k are the single-qubit Pauli operators $\sigma_k = \{I, X, Y, Z\}$ with $k = 0, 1, 2, 3$. For the single-qubit case, we give the more general channel to capture the asymmetric case found for the errors induced during midcircuit

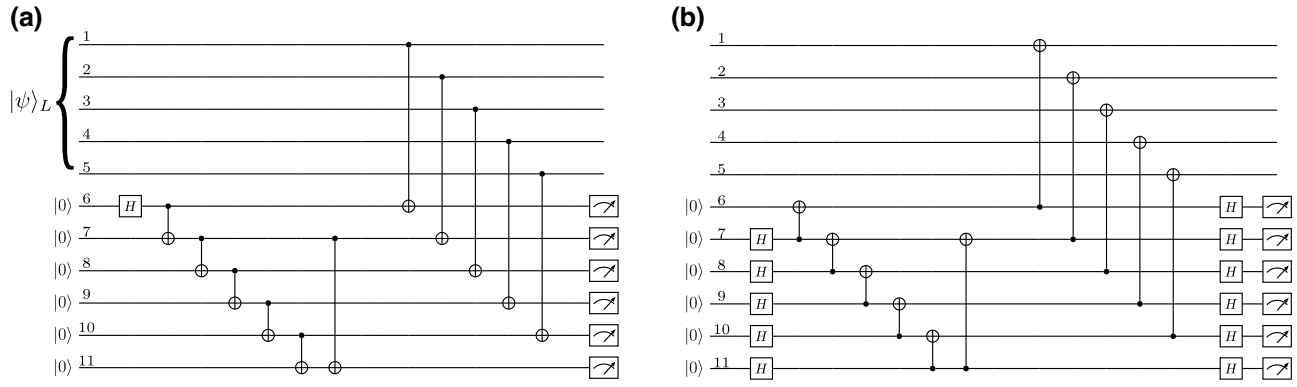

FIG. 11. Circuits for Steane-type syndrome extraction in the repetition code. Syndrome extraction for the (a) bit-flip code or (b) phase-flip code is performed by initializing a logical auxiliary qubit in a suitable GHZ state on qubits 6–10 and verifying it with an additional flag qubit 11. Sequentially, a transversal CNOT gate is applied and the auxiliary qubit is measured in the corresponding basis. The flag verification (qubit 11) can be left out in the circuits for the respective distance-3 codes without breaking fault tolerance.

TABLE III. The error rates and duration of operations on a trapped-ion quantum processor. These values correspond to the trapped-ion setup that has been used in the experiments and are used in the following simulations. The gate durations are increased by 10 µs compared to the values given in Appendix C to account for settling times of the addressing optics, when the ion being addressed is changed.

Operation	Error rate	Duration (µs)
Two-qubit gate	$p_{2q} = 0.027$	322.5
Single-qubit gate	$p_{1q} = 0.0036$	25
Measurement	$p_{\text{meas}} = 0.003$	
Preparation	$p_{\text{init}} = 0.003$	
Midcircuit detection	$p^{(x)}_{\text{midcirc}} = 0.011$ $p^{(y)}_{\text{midcirc}} = 0.024$ $p^{(z)}_{\text{midcirc}} = 0.035$	

measurements. The general formula reduces to the symmetric depolarizing case by choosing all three Pauli errors with equal probability $p_j = p_{1q}/3$, as we do for the single-qubit gate error. The parameters p_{1q} and p_{2q} specify the probability that any one of the errors of the corresponding error set occurs on the qubits that are acted upon. The qubits are initialized and measured in the computational basis. Faults on these operations are modeled by applying X errors after state preparations and before measurements with a probability p_{init} and p_{meas}, respectively. Furthermore, we include noise on idling qubits, which are not acted upon with a gate at a given step of the protocol. Since the dominant noise on idling qubits is dephasing due to magnetic field fluctuations, which limits the decoherence time $T_2 \approx 50$ ms, we model the noise channel for idling qubits by Pauli-Z faults as

$$\mathcal{E}_{\text{idle}}(\rho) = (1 - p_{\text{idle}})\rho + p_{\text{idle}} Z\rho Z. \tag{B3}$$

The probability p_{idle} of a Z fault on each idling qubit depends on the execution time t of the performed gate and is given by

$$p_{\text{idle}} = \frac{1}{2}\left[1 - \exp\left(-\frac{t}{T_2}\right)\right]. \tag{B4}$$

Midcircuit detections are performed in order to perform multiple rounds of error correction, where auxiliary qubits are measured while keeping the data qubits intact. The idling data qubits experience noise during this midcircuit detection, which we model as an asymmetric depolarizing channel on all data qubits. We estimate the individual Pauli $p^{(x)}_{\text{midcirc}}$, $p^{(y)}_{\text{midcirc}}$, and $p^{(z)}_{\text{midcirc}}$ error rates in this channel based on single-qubit process tomography. All error rates and gate times are summarized in Table III.

For the extrapolation to the limiting case of small gate error rates, we additionally perform simulations with a technique known as fault-path counting [46]. The goal here is to determine the leading-order contributions to the logical infidelity at low physical error rates. Since single faults cannot lead to logical errors by design, this function will be dominated by second-order terms when expanding as a polynomial of physical error rates. We focus on the gate errors p_{2q} and p_{1q} and set all other error sources to zero. This implies that the leading terms of the function describing the infidelity can be written as $\text{infid}(p_{2q}, p_{1q}) = c_2 p_{2q}^2 + c_1 p_{1q}^2 + c_{12} p_{1q} p_{2q} + \mathcal{O}(p^3)$. The coefficients c_i are related to the number of corresponding fault configurations resulting in logical failure. For example, c_2 is the sum over all configurations where placing faults on any two two-qubit gates in a given circuit (sequence) results in a logical error—and analogously for c_1 when placing two faults on any two single-qubit gates and for c_{12} when placing one two-qubit gate and one single-qubit gate fault. The coefficients furthermore contain a normalization, since we write the polynomial as a function of p_{1q} and p_{2q}, which determine the microscopic fault probabilities of a single-qubit gate fault as $p_{1q}/3$ and a two-qubit gate fault as $p_{2q}/15$ via Eq. (B1). To determine the logical outcome, each fault configuration has to be propagated to the end of the circuit. Fault-path counting is viable at low physical error rates when higher-order contributions are negligible. In this regime, this allows us to determine the coefficients of the polynomial such that we can explore the influence of different error sources. The coefficients are given in Table IV. As shown in Fig. 10, we compare the Steane and flagged syndrome readout schemes and plot the ratio of infidelities as a function of the single- and two-qubit gate error strength. We find that there are two regimes in which either method is preferable. Strikingly, for systems dominated by the two-qubit gate error $p_{2q} \gg p_{1q}$, our results show an advantage of Steane over flagged syndrome readout across the board.

TABLE IV. The coefficients obtained by fault-path counting simulations. As described in the main text, c_k related to the number of fault configurations of two faults leading to a logical error weighted with the probability of occurrence. These coefficients determine the leading order of the polynomial describing the infidelity of each error-correction scheme at low error rates.

	c_2	c_1	c_{12}
Steane EC	70.3	684.2	438.3
Flagged EC	204.5	178.7	543.6

APPENDIX C: EXPERIMENTAL METHODS

All of the experiments presented in this paper have been conducted on a trapped-ion quantum processor [47]. In a nonsegmented macroscopic Paul trap, a string of 16 $^{40}Ca^{+}$ ions is trapped, with interion spacing ranging from 3.8 to 6.0 µm, set by trap parameters. The center-of-mass modes of the ion string in the pseudoharmonic potential of the trap have oscillation frequencies of $\omega_z = 2\pi \times 369$ kHz, $\omega_x = 2\pi \times 3086$ kHz, and $\omega_y = 2\pi \times 3165$ kHz

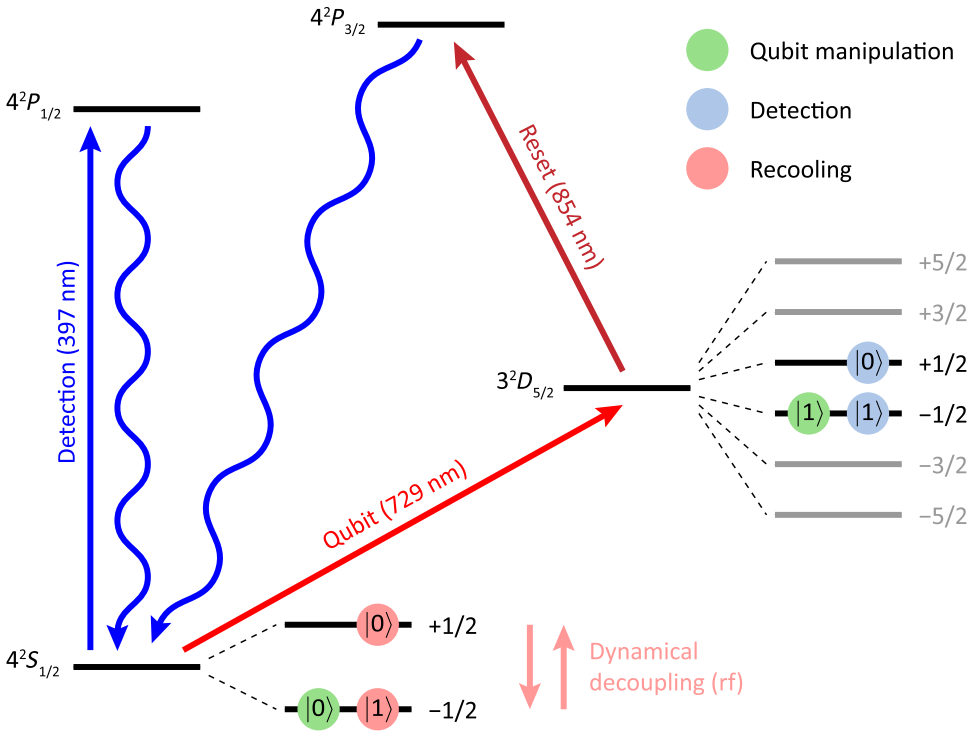

FIG. 12. The energy scheme of $^{40}Ca^+$. Lasers at wavelengths of 729, 854, and 397 nm are used for qubit manipulation, qubit reset, and Doppler cooling, respectively. Different encodings are used for the data qubits in different stages of a circuit. Gates are applied to the optical qubit encoding (green symbols). For midcircuit measurements, the data qubits are encoded in different Zeeman sublevels of the states $|0\rangle = |4^2S_{1/2}\rangle$ and $|0\rangle = |3^2D_{5/2}\rangle$ to avoid interaction with laser light for qubit-state detection, reset, and recooling illuminating the whole register. Furthermore, an rf drive is available for dynamical decoupling when the qubit is encoded in the Zeeman manifold of the electronic ground state during the side-band-recooling stage of the midcircuit measurements.

for the direction along the ion string (referred to as axial) and the two perpendicular directions (referred to as radial), respectively. The first step of every experimental cycle is a Doppler-cooling pulse acting on the $|4^2S_{1/2}\rangle \leftrightarrow |4^2P_{1/2}\rangle$ transition at a wavelength of 397 nm (see Fig. 12), with a duration of 500 µs. Simultaneously, the ion chain is illuminated with light at 866 nm to avoid pumping to the dark state $|3^2D_{3/2}\rangle$ by driving any population trapped there back to the state $|4^2S_{1/2}\rangle$. Both laser beams act on all ions simultaneously and have spatial overlap with all motional modes. The two lowest-frequency axial modes and all 32 radial modes are further cooled close to the ground state by resolved side-band cooling [27]. The ions are illuminated by a laser beam red detuned by the respective motional frequency from the $|4^2S_{1/2}, m_J = -1/2\rangle \leftrightarrow |3^2D_{5/2}, m_J = -5/2\rangle$ transition at 729 nm. For the axial modes, the 729 nm laser propagates along the ion string, whereas the radial modes are cooled by a steerable addressed 729-nm beam illuminating only one ion at a time from a direction perpendicular to the ion string. To cool the radial modes, the ion having the strongest coupling to the respective motional mode is illuminated. All modes within approximately 50 kHz from the laser frequency are cooled, which allows us to cool 34 modes with only 15 frequency settings. To accelerate the cooling process, ions excited to the $|3^2D_{5/2}\rangle$ state are pumped to the state $|4^2P_{3/2}\rangle$ using laser light at 854 nm, from where they rapidly decay to one of the ground states. This side-band-cooling cycle is repeated up to five times depending on the mode, where one cycle takes 500 µs. The mean phonon number of the center-of-mass mode with mode frequency $\omega_y = 2\pi \times 3165$ kHz after side-band cooling is $\bar{n} = 0.05(1)$ and exhibits a heating rate of 3.6(2) phonons per second. For the rocking mode along the same direction, the mode closest in frequency to the center-of-mass mode with a relative detuning of 23 kHz, the mean phonon number after side-band cooling is $\bar{n} = 0.02(1)$. Within 50 ms, no heating is observed on this mode. This behavior is expected in macroscopic ion traps, as in such traps typically the noise leading to motional heating is spatially correlated along the ion string [48]. Measurement of the mean phonon number and heating rate for other motional modes is not trivial due to the crowding of the modes in frequency space. However, we assume that the contribution of those modes to the entangling-gate dynamics is negligible. The finalizing

step of the state-preparation procedure is to prepare all ions in $|4^2S_{1/2}, m_J = -1/2\rangle$ by exciting the transition $|4^2S_{1/2}, m_J = +1/2\rangle \leftrightarrow |3^2D_{5/2}, m_J = +1/2\rangle$ with axial 729-nm light while speeding up the decay to the ground state using 854-nm light, as for side-band cooling.

The coherent manipulation of the individual qubits in the register subsequent to state preparation is exclusively done via tightly focused laser pulses with a propagation direction perpendicular to the ion string addressing the qubit transition $|4^2S_{1/2}, m_J = -1/2\rangle \leftrightarrow |3^2D_{5/2}, m_J = -1/2\rangle$. The experimental setup allows us to illuminate up to two ions simultaneously. Addressing a single ion i with light resonant to the qubit transition allows us to implement operations of the form $R_\phi^{(i)}(\theta) = \exp(-\mathrm{i}(\theta/2)(\sigma_x^{(i)}\cos\phi + \sigma_y^{(i)}\sin\phi))$, where the $\sigma_\bullet$ are single-qubit Pauli matrices. The rotation axis ϕ can be controlled via the light phase and the rotation angle θ via the light intensity and pulse duration. The duration of a pulse with $\theta = \pi/2$ is 15 µs. Together with virtual Z rotations [49], this operation allows us to implement arbitrary single-qubit unitary operations. The gate set is completed by adding the entangling Mølmer-Sørensen interaction, where any two ions may be illuminated with bichromatic light slightly detuned from the motional side bands corresponding to the radial mode at frequency ω_y [50]. Adjustment of the gate time to $t_{\mathrm{gate}} = 1/\delta = 312.5\,\mu\mathrm{s}$, where δ is the detuning from the motional side bands, implements the gate $\mathrm{MS}^{(ij)} = \exp(-\mathrm{i}(\pi/4)\sigma_x^{(i)}\sigma_x^{(j)})$, which is equivalent to the CNOT gate up to single-qubit rotations [51]. Qubit-state readout after application of a gate sequence to the qubit register is implemented by simultaneously illuminating the whole register with laser light at wavelengths of 397 and 866 nm. While qubits projected to the computational state $|0\rangle = |4^2S_{1/2}, m_J = -1/2\rangle$ repeatedly emit photons at a wavelength of 397 nm after being excited to $|4^2\mathrm{P}_{1/2}\rangle$ and returning to $|4^2S_{1/2}\rangle$, qubits projected to $|1\rangle = |4^2D_{5/2}, m_J = -1/2\rangle$ are not affected by those light fields and do not emit photons [27]. The imaging of the ion string on an electron multiplying charge-coupled device (EMCCD) camera allows for the spatially resolved detection of light emission from the ion string and therefore the computational-basis bit string into which the qubit register was projected can be reconstructed.

The error rates for the single-qubit gates are estimated from single-qubit randomized benchmarking on the 16-qubit register. We find an error rate per gate averaged over all 16 qubits of 0.0036, with a standard deviation of 0.0004. The two-qubit error rate is estimated by preparing a 16-qubit GHZ state and comparing the experimentally measured fidelity to simulated fidelities from numerical simulations, accounting for errors on single-qubit gates, two-qubit gates, initialization, and measurements. As outlined in our previous work [52], for the analysis of the fidelity of the prepared GHZ state we perform two measurements: the probabilities for projection to one of the two basis states $|0\rangle^{\otimes 16}$ and $|1\rangle^{\otimes 16}$ are determined by a direct projective measurement in the Z basis after preparation. The off-diagonal elements of the density matrix of the GHZ state are, instead, measured by applying single-qubit gates $R_\varphi^{(i)}(\pi/2)$ to all qubits after preparing the GHZ state. For different phases φ, the parity of the prepared state is measured via a projective measurement and a sinusoidal model is fitted to the observed parity oscillations [53]. The mean of the sum of the populations in $|0\rangle^{\otimes 16}$ and $|1\rangle^{\otimes 16}$ and the contrast of the parity oscillations of the coherence measurement gives the fidelity of the GHZ state. Averaging over multiple instances of the prepared GHZ state over the course of around 13 h gives a mean fidelity of 0.54 with a standard deviation of 0.04, corresponding to an estimated two-qubit error rate $p_{2q} = 0.027$ with a standard deviation of 0.005. Typical values for qubit initialization and measurement fault rates are $p_{\mathrm{init}} = p_{\mathrm{meas}} = 0.003$ in the device under consideration [27].

1. Midcircuit measurements

For midcircuit measurements, only a part of the register, referred to as the auxiliary qubits, is supposed to be projected into the computational basis, while another part of the register, referred to as the data qubits, is ideally unaffected. To avoid projecting the data qubits, their qubit encoding is transferred to $|0\rangle_{\mathrm{data,\,det}} = |3^2D_{5/2}, m_J = +1/2\rangle$ and $|1\rangle_{\mathrm{data,\,det}} = |3^2D_{5/2}, m_J = -1/2\rangle$ by first applying an rf pulse with a pulse area of π (a π pulse) that transfers the population in $|4^2S_{1/2}, m_J = -1/2\rangle$ to $|4^2S_{1/2}, m_J = +1/2\rangle$ followed by a π pulse on the transition $|4^2S_{1/2}, m_J = +1/2\rangle \leftrightarrow |3^2D_{5/2}, m_J = +1/2\rangle$ for all data qubits. Subsequently, the same detection pulse as for the final detection is applied. Recoil of scattered photons from bright auxiliary qubits heats up the ion string, which would lead to reduced gate fidelities after the midcircuit measurement. Therefore, a Doppler-cooling pulse is applied. To recool the ion string close to the motional ground state, an additional side-band-cooling step is necessary. The data-qubit encoding is transferred to $|0\rangle_{\mathrm{data,\,cool}} = |4^2S_{1/2}, m_J = +1/2\rangle$ and $|1\rangle_{\mathrm{data,\,cool}} = |4^2S_{1/2}, m_J = -1/2\rangle$ by applying π pulses on the transitions associated with the states $|4^2S_{1/2}, m_J = \pm 1/2\rangle$ and $|3^2D_{5/2}, m_J = \pm 1/2\rangle$, as side-band cooling involves illuminating the ion string with 854-nm light, which would otherwise destroy any information encoded in the $|3^2D_{5/2}\rangle$ manifold. Then, the same side-band-cooling pulse scheme as for state preparation is applied, apart from the fact that axial modes are not cooled and ions encoding data qubits are excluded from the set of allowed cooling ions. The cooling of axial modes would require using the axial 729-nm beam, as the addressed beam does

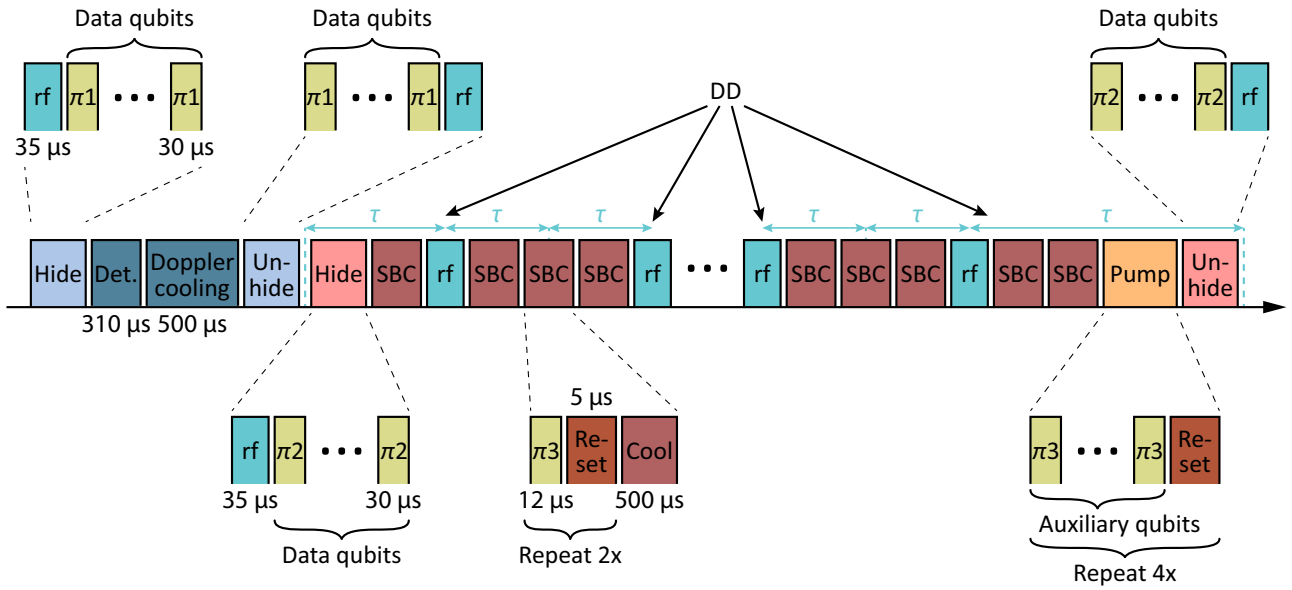

FIG. 13. The sequence-timing diagram of a midcircuit measurement. The first light blue pulse, labeled "Hide", transfers the encoding of the data qubits from the encoding labeled with green symbols in Fig. 12 to the encoding labeled with blue symbols. Instead of directly applying a π pulse labeled "π_1" on the transition $|4^2S_{1/2}, m_J = -1/2\rangle \leftrightarrow |3^2D_{5/2}, m_J = +1/2\rangle$, an rf pulse with pulse area π followed by π pulses on the transition $|4^2S_{1/2}, m_J = +1/2\rangle \leftrightarrow |3^2D_{5/2}, m_J = +1/2\rangle$ are applied. As the coupling on the $\delta m_J = 0$ transition is significantly higher, this allows us to speed up the hiding process. After applying detection and Doppler-cooling pulses, the encoding of the data qubits is returned to the encoding shown with green symbols by applying the reverted hiding sequence. Subsequently, the encoding of the data qubits is transferred to the encoding shown with red symbols by applying an rf pulse with pulse area π followed by π pulses labeled "π_2" on the transition $|4^2S_{1/2}, m_J = -1/2\rangle \leftrightarrow |3^2D_{5/2}, m_J = -1/2\rangle$. Although the two rf pulses implement the identity, we do not omit them to retain symmetry with the unhiding pulses at the end of the sequence. Before each side-band-cooling cycle, a π pulse labeled "π_3" on the transition $|4^2S_{1/2}, m_J = -1/2\rangle \leftrightarrow |3^2D_{5/2}, m_J = -1/2\rangle$ is applied to the auxiliary qubit used for cooling in the respective side-band-cooling cycle. Subsequently, a pulse labeled "Reset" (simultaneous illumination with 854- and 866-nm light of the entire register) is applied. Together, these two pulses ensure that the auxiliary-qubit population is transferred to $|4^2S_{1/2}, m_J = -1/2\rangle$ and side-band cooling can operate efficiently. After the last side-band-cooling cycle, all auxiliary qubits that are supposed to be reused are reinitialized to $|4^2S_{1/2}, m_J = -1/2\rangle$ using the same pulse sequence that optically pumps the population before each side-band-cooling cycle. The midcircuit measurement procedure is concluded with the unhiding sequence returning the data-qubit encoding to the encoding labeled with green symbols in Fig. 12. In between side-band-cooling cycles, rf pulses are applied for dynamical decoupling. The length of the pulse labeled "Cool" is varied for the first and last side-band-cooling cycle to ensure that the refocusing time τ is kept constant for hiding and pumping sequences involving different data-qubit and auxiliary-qubit numbers.

not have overlap with the direction of motion of axial modes, and therefore would also affect data qubits. Prior to every side-band-cooling pulse, the respective ion is pumped to $|4^2S_{1/2}, m_J = -1/2\rangle$ by applying two repetitions of a π pulse on the transition $|4^2S_{1/2}, m_J = +1/2\rangle \leftrightarrow |3^2D_{5/2}, m_J = -3/2\rangle$ followed by a 5 µs pulse of 854-nm light. The midcircuit measurement is finalized by repeating the pumping cycle for all auxiliary qubits that are supposed to be reused four times and restoring the encoding of the data qubits by applying a π pulse on the transition $|4^2S_{1/2}, m_J = -1/2\rangle \leftrightarrow |3^2D_{5/2}, m_J = -1/2\rangle$ followed by an rf π pulse transferring the population in $|4^2S_{1/2}, m_J = +1/2\rangle$ to $|4^2S_{1/2}, m_J = -1/2\rangle$. The midcircuit side-band-cooling procedure requires around 15 ms. A detailed time line of a midcircuit measurement is shown in Fig. 13.

2. Dynamical decoupling

The coherence time in the optical-qubit encoding and the ground-state encoding is on the order of 50 and 5 ms, respectively. Idling data qubits would thus suffer from significant dephasing during side-band cooling if no countermeasures were taken. Therefore, a dynamical decoupling sequence is performed on the data qubits during the recooling procedure to preserve coherence. This decoupling is implemented with an rf antenna radiating at 16.7 MHz, acting on the entire register simultaneously, which drives the transition between the two ground states, where the data qubits are encoded during side-band cooling. The antenna, with a diameter of about 2 cm, is connected to a resonant circuit and is mounted outside the vacuum chamber, as close as possible to the

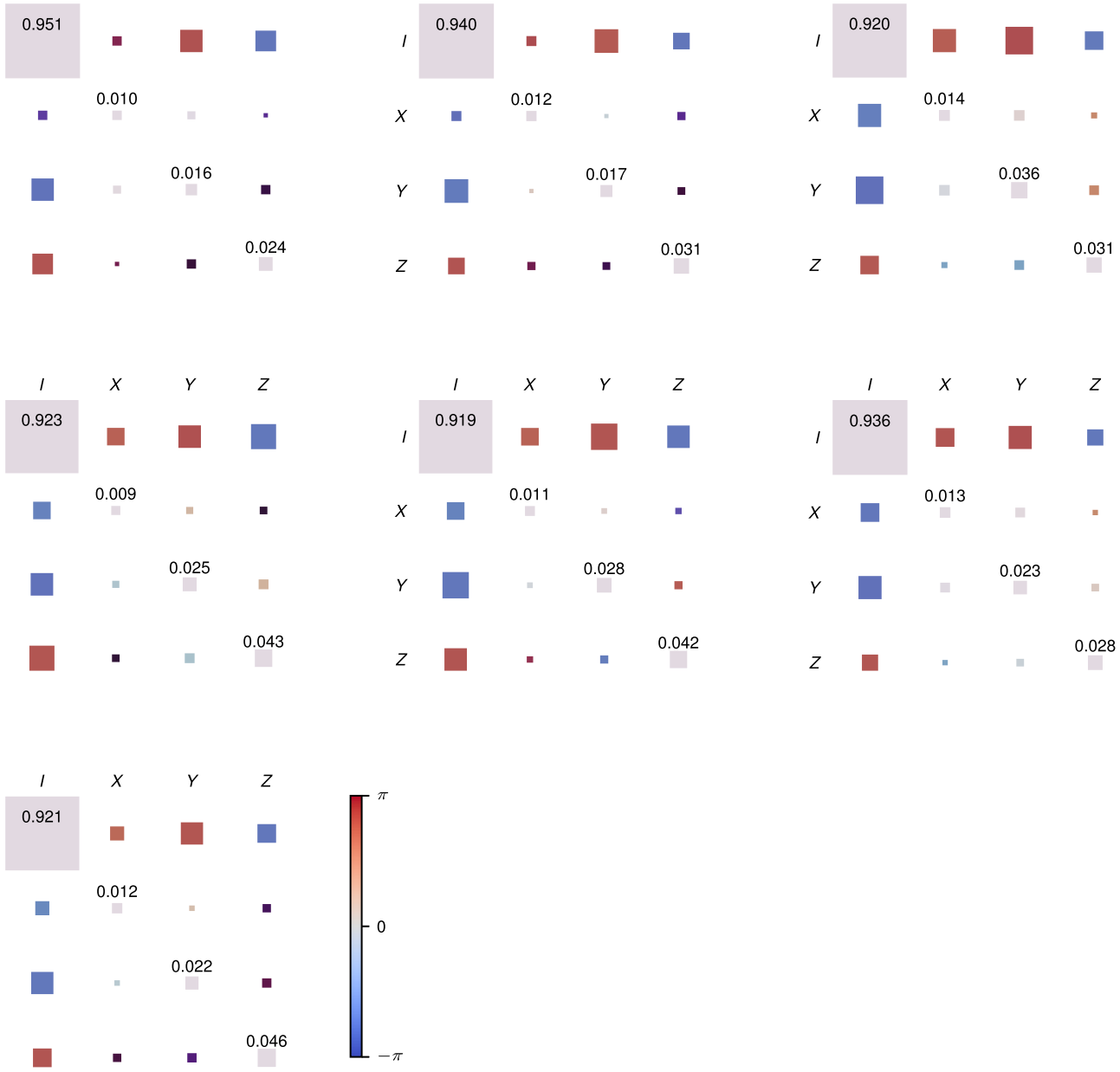

FIG. 14. Single-qubit process tomography of midcircuit measurements. The chi-matrix representation of the process acting on data qubits during midcircuit measurements is shown for all data qubits individually. The process fidelity ranges from 0.919 to 0.951, with an average of 0.930 and a standard deviation of 0.011. The area and the color coding of the squares correspond to the absolute value and the phase of the elements of the chi matrix, respectively.

ion string. Driving the resonant antenna with a power of approximately 2 W allows us to implement a bit flip in 35 μs. The maximum relative deviation in Rabi frequency in the 16-qubit register is $(\Omega_{\max} - \Omega_{\min})/\Omega_{\min} = 0.002(1)$, where $\Omega_{\max}$ and $\Omega_{\min}$ are the maximum and minimum Rabi frequencies, respectively. The rf source driving the antenna is a direct digital synthesizer integrated in the same control hardware that also generates the rf pulses driving the acousto-optical modulators used to address the optical-qubit transition. The phase of the pulses generated by these rf sources is defined with respect to a common reference, enabling coherent operation across different direct digital synthesizer channels. A decoupling pulse is applied approximately every millisecond in between cooling pulses for different motional modes. Under the application of this decoupling scheme, we do not see any significant dephasing up to a waiting time of 60 ms, which indicates an effective coherence time larger than 1 s. The effect of a full midcircuit measurement on the data qubits is characterized via single-qubit process

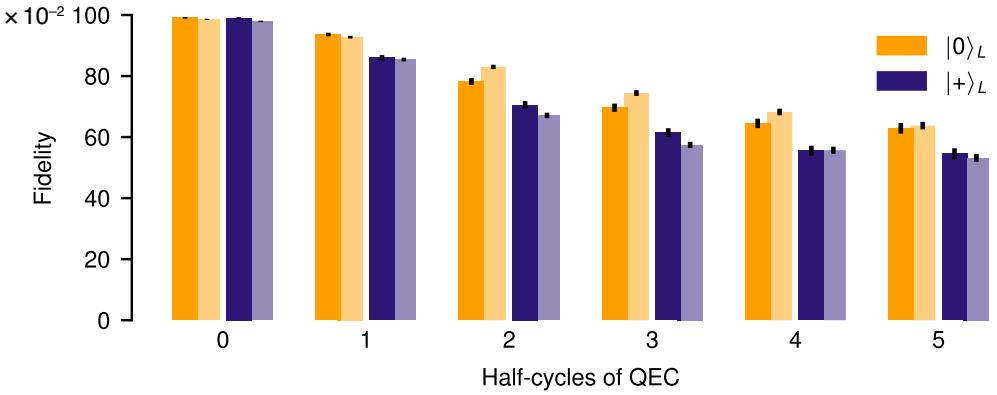

FIG. 15. Logical fidelities for half-cycles of syndrome extraction on the seven-qubit color code: logical fidelities obtained from Steane-type QEC for the logical input states $|0\rangle_L$ and $|+\rangle_L$. For the input states $|0\rangle_L$ and $|+\rangle_L$, only the syndrome given by the Z- and X-type stabilizer generators, respectively, is extracted multiple times. Half-cycle 0 corresponds to the encoding of the logical state with no extra round of QEC. The experimental and simulation results are depicted with darker and lighter shades, respectively.

tomography of the data qubits using linear reconstruction. In Fig. 2(c), we show the chi-matrix representation [19] of the process averaged over all data qubits in the Pauli basis, whereas in Fig. 14, we show the underlying process matrices for the individual data qubits. The average fidelity is 0.930, with a standard deviation of 0.011. The averaged process matrix data is also used to inform the error model described in Appendix B, as there are no salient differences between the individual matrices. These error probabilities are extracted from the experimental process matrix, quantifying the effect of midcircuit measurements on data qubits, shown in Fig. 2(c).

The dynamical decoupling scheme described above can only be applied when the data qubits are encoded in the ground state, shown with red symbols in Fig. 12. For detection and Doppler cooling, the data qubits are transferred to the encoding shown with blue symbols, which is a factor of approximately $\frac{2}{1.2}$ less sensitive to magnetic field fluctuations compared to the ground-state encoding given by the g factors of the states $|4^2S_{1/2}\rangle$ and $|3^2D_{5/2}\rangle$. Therefore, assuming a coherence time $T_2 = 8\,\mathrm{ms}$ limited by magnetic field fluctuations and an idling duration of 0.8 ms, the dephasing error probability of the data qubits during detection and Doppler cooling of the auxiliary qubits is 0.05 according to Eq. B4. Increasing the coherence time to $T_2 = 1\,\mathrm{s}$ would decrease the error rate on the data qubits to 0.0004. It is likely that another major contribution to the overall error affecting data qubits during midcircuit measurements is crosstalk of hiding pulses, where the Rabi frequency of undesired crosstalk is on the order of 100 times smaller than the Rabi frequency on the target ion. Mitigating the effect of hiding pulses on neighboring ions using composite pulses together with an extended coherence time could significantly reduce the error rate on data qubits for midcircuit measurements.

APPENDIX D: UNCERTAINTY ESTIMATION

The uncertainties given in this work account for statistical errors under the assumption of an underlying binomial distribution of the measurement outcomes. We make use of the Wilson score interval [54] in order to obtain error intervals in the range $[0, 1]$ even for probabilities close to 0 or 1. The upper (referred to as "+" in the formula) and lower ("−") bound of the interval for a probability p measured with N shots are given by

$$p_\pm(p) = \frac{1}{1+\frac{z(\alpha)^2}{N}} \times \left(p + \frac{z(\alpha)^2}{2N} \pm z(\alpha)\sqrt{\frac{p(1-p)}{N} + \frac{z(\alpha)^2}{4N^2}}\right), \tag{D1}$$

where $z(\alpha) = \Phi^{-1}[1-(\alpha/2)]$, in which Φ^{-1} is the quantile function of the normal distribution and α is the target error rate. We choose $z = 1$, which corresponds to a confidence level of $1 - \alpha \approx 0.68$.

APPENDIX E: LOGICAL FIDELITY

The figure of merit for the quality of a logical state that we choose in this work is the logical fidelity, which is the probability of retrieving the correct logical state. A single logical qubit state ρ is given by

$$\rho = \frac{1}{2}\left(\sigma_0 + \langle X_L\rangle\sigma_1 + \langle Y_L\rangle\sigma_2 + \langle Z_L\rangle\sigma_3\right), \tag{E1}$$

where X_L, Y_L, and Z_L are the logical operators and the $\sigma_\bullet$ are single-qubit Pauli matrices. Then, the logical fidelity of ρ with respect to a logical target state ρ_t after performing

an ideal round of QEC is given by

$$\mathcal{F}_t(\rho) = \langle P_t \rangle = \mathrm{tr}\,(P_t \rho)\,, \tag{E2}$$

where P_t is the projector on the logical target state. For the logical Pauli states $|0\rangle_L$ and $|+\rangle_L$, the projectors read

$$P_{|0\rangle_L} = \frac{1}{2}\,(\mathbb{1} + Z_L) \quad \text{and} \quad P_{|+\rangle_L} = \frac{1}{2}\,(\mathbb{1} + X_L)\,, \tag{E3}$$

leading to the expressions

$$\mathcal{F}_{|0\rangle_L} = \frac{1}{2}\,(1 + \langle Z_L \rangle) \quad \text{and} \quad \mathcal{F}_{|+\rangle_L} = \frac{1}{2}\,(1 + \langle X_L \rangle) \tag{E4}$$

for the logical fidelities of the logical states considered in this work.

APPENDIX F: ADDITIONAL RESULTS

In addition to the implementation of multiple rounds of Steane QEC on the seven-qubit color code, we realize repetitive readout of a single type of stabilizer generator, corresponding to executing either the first or the second half of the scheme displayed in Fig. 1(c). The syndrome extraction is applied to a logical Pauli state sensitive to the corrections suggested by the syndrome measurement; e.g., Z-type stabilizer generators are measured for the input state $|0\rangle_L$ and X-type stabilizer generators are measured for the input state $|+\rangle_L$. We refer to one readout as a half-cycle of QEC. We implement up to five half-cycles of QEC, with the corresponding logical fidelities being shown in Fig. 15. Again, we see good agreement between the experiments and the data from the numerical simulations.

[1] Google Quantum AI, Exponential suppression of bit or phase errors with cyclic error correction, Nature **595**, 383 (2021).

[2] S. Krinner, N. Lacroix, A. Remm, A. Di Paolo, E. Genois, C. Leroux, C. Hellings, S. Lazar, F. Swiadek, J. Herrmann, G. J. Norris, C. K. Andersen, M. Müller, A. Blais, C. Eichler, and A. Wallraff, Realizing repeated quantum error correction in a distance-three surface code, Nature **605**, 669 (2022).

[3] Y. Zhao, *et al.*, Realization of an error-correcting surface code with superconducting qubits, Phys. Rev. Lett. **129**, 030501 (2022).

[4] Google Quantum AI, Suppressing quantum errors by scaling a surface code logical qubit, Nature **614**, 676 (2023).

[5] R. S. Gupta, N. Sundaresan, T. Alexander, C. J. Wood, S. T. Merkel, M. B. Healy, M. Hillenbrand, T. Jochym-O'Connor, J. R. Wootton, T. J. Yoder, A. W. Cross, M. Takita, and B. J. Brown, Encoding a magic state with beyond break-even fidelity, Nature **625**, 259 (2024).

[6] J. Hilder, D. Pijn, O. Onishchenko, A. Stahl, M. Orth, B. Lekitsch, A. Rodriguez-Blanco, M. Müller, F. Schmidt-Kaler, and U. G. Poschinger, Fault-tolerant parity readout on a shuttling-based trapped-ion quantum computer, Phys. Rev. X **12**, 011032 (2022).

[7] L. Egan, D. M. Debroy, C. Noel, A. Risinger, D. Zhu, D. Biswas, M. Newman, M. Li, K. R. Brown, M. Cetina, and C. Monroe, Fault-tolerant control of an error-corrected qubit, Nature **598**, 281 (2021).

[8] C. Ryan-Anderson, J. G. Bohnet, K. Lee, D. Gresh, A. Hankin, J. P. Gaebler, D. Francois, A. Chernoguzov, D. Lucchetti, N. C. Brown, T. M. Gatterman, S. K. Halit, K. Gilmore, J. A. Gerber, B. Neyenhuis, D. Hayes, and R. P. Stutz, Realization of real-time fault-tolerant quantum error correction, Phys. Rev. X **11**, 041058 (2021).

[9] L. Postler, S. Heußen, I. Pogorelov, M. Rispler, T. Feldker, M. Meth, C. D. Marciniak, R. Stricker, M. Ringbauer, R. Blatt, P. Schindler, M. Müller, and T. Monz, Demonstration of fault-tolerant universal quantum gate operations, Nature **605**, 675 (2022).

[10] C. Ryan-Anderson, N. C. Brown, M. S. Allman, B. Arkin, G. Asa-Attuah, C. Baldwin, J. Berg, J. G. Bohnet, S. Braxton, N. Burdick, *et al.*, Implementing fault-tolerant entangling gates on the five-qubit code and the color code, arXiv:2208.01863.

[11] D. H. Menendez, A. Ray, and M. Vasmer, Implementing fault-tolerant non-Clifford gates using the $[\![8, 3, 2]\!]$ color code, arXiv:2309.08663.

[12] Y. Wang, S. Simsek, T. M. Gatterman, J. A. Gerber, K. Gilmore, D. Gresh, N. Hewitt, C. V. Horst, M. Matheny, T. Mengle, B. Neyenhuis, and B. Criger, Fault-tolerant one-bit addition with the smallest interesting colour code, arXiv:2309.09893.

[13] B. Pokharel and D. A. Lidar, Better-than-classical Grover search via quantum error detection and suppression, npj Quantum Inf. **10**, 23 (2024).

[14] D. Bluvstein, *et al.*, Logical quantum processor based on reconfigurable atom arrays, Nature **626**, 58 (2023).

[15] A. M. Steane, Active stabilization, quantum computation, and quantum state synthesis, Phys. Rev. Lett. **78**, 2252 (1997).

[16] P. W. Shor, in *Proceedings of 37th Conference on Foundations of Computer Science* (IEEE, Burlington, VT, USA, 1996), p. 56.

[17] C. Chamberland and M. E. Beverland, Flag fault-tolerant error correction with arbitrary distance codes, Quantum **2**, 53 (2018).

[18] B. W. Reichardt, Fault-tolerant quantum error correction for Steane's seven-qubit color code with few or no extra qubits, Quantum Sci. Technol. **6**, 015007 (2020).

[19] M. A. Nielsen and I. L. Chuang, *Quantum Computation and Quantum Information* (Cambridge University Press, Cambridge, 2010).

[20] V. Negnevitsky, M. Marinelli, K. K. Mehta, H. Y. Lo, C. Flühmann, and J. P. Home, Repeated multi-qubit readout and feedback with a mixed-species trapped-ion register, Nature **563**, 527 (2018).

[21] J. M. Pino, J. M. Dreiling, C. Figgatt, J. P. Gaebler, S. A. Moses, M. S. Allman, C. H. Baldwin, M. Foss-Feig, D. Hayes, K. Mayer, C. Ryan-Anderson, and B. Neyenhuis,

Demonstration of the trapped-ion quantum CCD computer architecture, Nature **592**, 209 (2021).

[22] S. D. Erickson, J. J. Wu, P. Y. Hou, D. C. Cole, S. Geller, A. Kwiatkowski, S. Glancy, E. Knill, D. H. Slichter, A. C. Wilson, and D. Leibfried, High-fidelity indirect readout of trapped-ion hyperfine qubits, Phys. Rev. Lett. **128**, 160503 (2022).

[23] D. Zhu, G. D. Kahanamoku-Meyer, L. Lewis, C. Noel, O. Katz, B. Harraz, Q. Wang, A. Risinger, L. Feng, D. Biswas, L. Egan, A. Gheorghiu, Y. Nam, T. Vidick, U. Vazirani, N. Y. Yao, M. Cetina, and C. Monroe, Interactive cryptographic proofs of quantumness using mid-circuit measurements, Nat. Phys. **19**, 1725 (2023).

[24] M. Riebe, T. Monz, K. Kim, A. Villar, P. Schindler, M. Chwalla, M. Hennrich, and R. Blatt, Deterministic entanglement swapping with an ion-trap quantum computer, Nat. Phys. **4**, 839 (2008).

[25] T. Monz, D. Nigg, E. A. Martinez, M. F. Brandl, P. Schindler, R. Rines, S. X. Wang, I. L. Chuang, and R. Blatt, Realization of a scalable Shor algorithm, Science **351**, 1068 (2016).

[26] T. Manovitz, Y. Shapira, L. Gazit, N. Akerman, and R. Ozeri, Trapped-ion quantum computer with robust entangling gates and quantum coherent feedback, PRX Quantum **3**, 010347 (2022).

[27] P. Schindler, D. Nigg, T. Monz, J. T. Barreiro, E. Martinez, S. X. Wang, S. Quint, M. F. Brandl, V. Nebendahl, C. F. Roos, M. Chwalla, M. Hennrich, and R. Blatt, A quantum information processor with trapped ions, New J. Phys. **15**, 123012 (2013).

[28] H. Y. Carr and E. M. Purcell, Effects of diffusion on free precession in nuclear magnetic resonance experiments, Phys. Rev. **94**, 630 (1954).

[29] S. Meiboom and D. Gill, Modified spin-echo method for measuring nuclear relaxation times, Rev. Sci. Instrum. **29**, 688 (1958).

[30] J. Kelly, *et al.*, State preservation by repetitive error detection in a superconducting quantum circuit, Nature **519**, 66 (2015).

[31] E. Knill, Quantum computing with realistically noisy devices, Nature **434**, 39 (2005).

[32] A. Steane, Multiple-particle interference and quantum error correction, Proc. Phys. Soc. A **452**, 2551 (1996).

[33] H. Bombin and M. A. Martin-Delgado, Topological quantum distillation, Phys. Rev. Lett. **97**, 180501 (2006).

[34] D. Nigg, M. Mueller, E. A. Martinez, P. Schindler, M. Hennrich, T. Monz, M. A. Martin-Delgado, and R. Blatt, Quantum computations on a topologically encoded qubit, Science **345**, 302 (2014).

[35] H. Goto, Minimizing resource overheads for fault-tolerant preparation of encoded states of the Steane code, Sci. Rep. **6**, 19578 (2016).

[36] T. P. Harty, D. T. C. Allcock, C. J. Ballance, L. Guidoni, H. A. Janacek, N. M. Linke, D. N. Stacey, and D. M. Lucas, High-fidelity preparation, gates, memory, and readout of a trapped-ion quantum bit, Phys. Rev. Lett. **113**, 220501 (2014).

[37] T. Ruster, C. T. Schmiegelow, H. Kaufmann, C. Warschburger, F. Schmidt-Kaler, and U. G. Poschinger, A long-lived Zeeman trapped-ion qubit, Appl. Phys. B **122**, 254 (2016).

[38] P. Wang, C. Y. Luan, M. Qiao, M. Um, J. Zhang, Y. Wang, X. Yuan, M. Gu, J. Zhang, and K. Kim, Single ion qubit with estimated coherence time exceeding one hour, Nat. Commun. **12**, 233 (2021).

[39] S. Wimperis, Composite pulses with rectangular excitation and inversion profiles, J. Magn. Reson. **83**, 509 (1989).

[40] S. Wimperis, Broadband, narrowband, and passband composite pulses for use in advanced NMR experiments, J. Magn. Reson. **109**, 221 (1994).

[41] https://doi.org/10.5281/zenodo.10390470

[42] P. Aliferis, D. Gottesman, and J. Preskill, Quantum accuracy threshold for concatenated distance-3 codes, Quantum Inf. Comput. **6**, 97 (2006).

[43] C. Chamberland, Ph.D. thesis, Department of Physics & Astronomy, University of Waterloo, 2018.

[44] C. Gidney, STIM: A fast stabilizer circuit simulator, Quantum **5**, 497 (2021).

[45] C. Ryan-Anderson, Ph.D. thesis, Department of Physics & Astronomy, The University of New Mexico, 2018.

[46] A. V. Rynbach, A. Muhammad, A. C. Mehta, J. Hussmann, and J. Kim, A quantum performance simulator based on fidelity and fault-path counting, arXiv:1212.0845.

[47] I. Pogorelov, T. Feldker, C. D. Marciniak, L. Postler, G. Jacob, O. Krieglsteiner, V. Podlesnic, M. Meth, V. Negnevitsky, M. Stadler, B. Höfer, C. Wächter, K. Lakhmanskiy, R. Blatt, P. Schindler, and T. Monz, Compact ion-trap quantum computing demonstrator, PRX Quantum **2**, 020343 (2021).

[48] M. Brownnutt, M. Kumph, P. Rabl, and R. Blatt, Ion-trap measurements of electric-field noise near surfaces, Rev. Mod. Phys. **87**, 1419 (2015).

[49] D. C. McKay, C. J. Wood, S. Sheldon, J. M. Chow, and J. M. Gambetta, Efficient Z gates for quantum computing, Phys. Rev. A **96**, 022330 (2017).

[50] A. Sørensen and K. Mølmer, Entanglement and quantum computation with ions in thermal motion, Phys. Rev. A **62**, 022311 (2000).

[51] D. Maslov, Basic circuit compilation techniques for an ion-trap quantum machine, New J. Phys. **19**, 023035 (2017).

[52] S. Heußen, L. Postler, M. Rispler, I. Pogorelov, C. D. Marciniak, T. Monz, P. Schindler, and M. Müller, Strategies for a practical advantage of fault-tolerant circuit design in noisy trapped-ion quantum computers, Phys. Rev. A **107**, 042422 (2023).

[53] T. Monz, P. Schindler, J. T. Barreiro, M. Chwalla, D. Nigg, W. A. Coish, M. Harlander, W. Hänsel, M. Hennrich, and R. Blatt, 14-Qubit entanglement: Creation and coherence, Phys. Rev. Lett. **106**, 130506 (2011).

[54] E. B. Wilson, Probable inference, the law of succession, and statistical inference, J. Am. Stat. Assoc. **22**, 209 (1927).